PAPER

Check for updates

Tuning cesium–guanidinium in formamidinium tin triiodide perovskites with an ethylenediammonium additive for efficient and stable lead-free perovskite solar cells†

Gabriella A. Tosado, Erjin Zheng [iD] and Qiuming Yu [iD] *

Achieving efficient and stable tin-based perovskite solar cells remains challenging. In this work, we incorporate the ethylenediammonium diiodide (EDAI$_2$) additive into a cesium–guanidinium doped formamidinium tin triiodide perovskite with the composition of (CsGA)$_x$FA$_{1−2x}$SnI$_3$ + y% EDAI$_2$. This new perovskite utilizes the strong hydrogen bonding of the guanidinium cation and the lattice strain relaxation of the small cesium cation as well as the hollowing and passivation effects of the EDAI$_2$ additive. The EDAI$_2$ additive not only yields pinhole-free cubic phase perovskite films but also decreases both shallow and deep trap states in the perovskite films. These effects are pronounced with the increase of substitution of the pair of GA$^+$ and Cs$^+$. The new perovskites are deployed in inverted planar solar cells. A maximum power conversion efficiency (PCE) of 5.01% is achieved with the (CsGA)$_{0.15}$FA$_{0.70}$SnI$_3$ + 0% EDAI$_2$ device but the device degrades after storage in a nitrogen-filled glove box for 30 days. Both performance and stability are improved with the addition of EDAI$_2$. A maximum PCE of 5.72% is achieved with the (CsGA)$_{0.15}$FA$_{0.70}$SnI$_3$ + 1.0% EDAI$_2$ device. The (CsGA)$_{0.15}$FA$_{0.70}$SnI$_3$ + 1.5% EDAI$_2$ devices exhibit a maximum PCE of 5.69% and the performance is further increased to 6.39% after storage in a nitrogen-filled glove box for 4 days; 70% of the initial PCE is retained after 45 days. This study demonstrates the benefit of tuning cation sizes and introducing divalent cations to integrate stabilizing factors into pure Sn perovskites, creating new routes for efficient and stable lead-free perovskite solar cells.

Introduction

Perovskite solar cells (PVSCs) have progressed rapidly in recent years. With the record power conversion efficiency (PCE) reaching 25.2%[1] and the potential for cost effective roll-to-roll printing capabilities, PVSCs are well positioned to encourage a transition to a clean energy economy. However, the toxicity of lead-based perovskite materials and the low stability and poor performance of lead-free perovskite alternatives present a challenge towards commercialization of perovskite technologies. Tin-based perovskites have been investigated as low-toxic alternatives to lead-based perovskites because tin has a comparable ionic radius (Sn^{2+}, 1.15 Å and Pb^{2+}, 1.19 Å)[2] and is also a group 14 metal, allowing Sn to maintain the crucial MX$_6$ octahedron.[3] Tin-based perovskites have certain intrinsic advantages over lead-based perovskites for photovoltaic devices such as a more favorable, comparably smaller bandgap, resulting in a higher Shockley–Queisser limit,

Department of Chemical Engineering, University of Washington, Seattle, WA 98195, USA. E-mail: qyu@u.washington.edu

† Electronic supplementary information (ESI) available. See DOI: 10.1039/d0ma00520g

and a more rapid charge carrier mobility.[4,5] Unfortunately, the main drawback of pure Sn perovskites is an oxidation reaction that hinders photovoltaic performance. Tin-containing PVSCs have been shown to degrade from the oxidation of Sn^{2+} to the more thermodynamically favored Sn^{4+}, even in inert atmospheres, due to the small activation energy for the oxidation reaction.[6,7] The high levels of self-p-doping caused by Sn^{4+} create a high defect density, also resulting in a low open-circuit voltage, V_{oc}.[8]

One strategy for improving the performance and stability of tin-based PVSCs has been focusing on A-site cation mixtures. Single A-site cation pure Sn perovskites, such as cesium tin triiodide (CsSnI$_3$), methylammonium tin triiodide (MASnI$_3$), and formamidinium tin triiodide (FASnI$_3$), have been thoroughly explored in previous studies.[9] Although CsSnI$_3$ was the first explored active layer for pure Sn PVSCs, it has been plagued with a low PCE and V_{oc} because of its small tolerance factor, creating an orthorhombic perovskite phase.[10,11] MASnI$_3$ PVSCs demonstrated promising performance with a PCE of 6%. However, the devices were unstable and had poor reproducibility because of poor film morphology and Sn oxidation.[12,13] FASnI$_3$ was hypothesized to be more stable against oxidation because of increased hydrogen bonding and a lower dipole moment, allowing it to

better rotate in the octahedral cage and interact with the halides.[9,14]

Recently, another organic cation has been demonstrated to further protect Sn against oxidation.[15] Guanidinium (GA⁺) cations have been used in Sn based PVSCs to improve performance and stability under ambient conditions. Due to the larger ionic radius of GA⁺ ($r = 2.78$ Å) compared with FA⁺ ($r = 2.53$ Å) and MA⁺ ($r = 1.80$ Å), density functional theory (DFT) calculations predict that cubic-phase GASnI₃ will have a shorter hydrogen bonding length and stronger interactions with the SnI_6 octahedron.[16] The higher amounts of bonded amines create a symmetrical structure in GA⁺ and a zero electric dipole moment, unlike FA⁺ and MA⁺, allowing for freer rotation of GA⁺ in the SnI_6 framework. The high hydrogen bonding capability and free rotation enable GA⁺ to effectively passivate under-coordinated iodide ions, resulting in longer carrier lifetimes and an increased V_{oc} because of the reduced recombination centers.[17] The capability of passivating under-coordinated iodide ions is particularly important for pure Sn perovskites because iodide vacancies induce the oxidation of Sn^{2+} to Sn^{4+}.[7] In addition, the incorporation of GA⁺ into FASnI₃ reduces the tendency of phase segregation because of the multiple hydrogen bonding sites. Therefore, GA⁺ is an excellent candidate for stabilizing mixed A-site Sn based perovskites. However, simply incorporating GA⁺ into $GA_{0.20}FA_{0.80}SnI_3$ perovskites yielded very low efficiency PVSCs with a PCE of 0.5% even though extra SnF_2 was added as a reducing agent.[15] This could be due to the increased local lattice strain created by introducing such a large organic cation. The increased local lattice strain has been theorized to be due to increasing point defect formation to relieve the strain.[18] The increased point defects could be the sites for oxidation and/or trap centers, affecting the performance of Sn-based PVSCs significantly.

One method that has been shown to "hollow" out three-dimensional (3D) perovskites and reduce lattice strain is introducing ethylenediammonium diiodide (EDAI₂). EDAI₂ has been explored as an A-site cation in 3D FASnI₃ and MASnI₃ perovskites.[19] Shallow trap states are localized in the crystal bulk structure and are located near the conduction or valence band edges. Deep trap states involve grain boundary defects and are located closer to the middle of the band gap.[20,21] The incorporation of such a large divalent cation results in not only the occupation of A-sites, but also the removal of B- and X-sites, reducing both bulk defects and shallow trap states. In addition, the divalent cations terminate crystal surfaces, reducing deep trap states at grain boundaries. The performance of FASnI₃ PVSCs improved from a PCE of 1.40% without EDAI₂ to 7.14% with 10% EDAI₂ and the efficiency was maintained after 1000 h for encapsulated devices.[19] It has been demonstrated that incorporating EDAI₂ into MASnI₃ lowers the electron trap state density and increases the carrier lifetime, which leads to an improvement of the device performance from a PCE of 0.17% without EDAI₂ to 5.49% with 15% EDAI₂.[22] The significant improvement of device performance and stability is attributed to the occupation of point defects inside the crystalline grains and the passivation of defects at grain boundaries by EDAI₂

cations, decreasing both shallow and deep trap states. Adding EDAI₂ to $FA_{0.80}GA_{0.20}SnI_3$ greatly enhanced the device performance from a PCE of 0.5% without EDAI₂ to the maximum PCE of 7.4% with 1% EDAI₂.[23] More interestingly, the PCE even increased to a maximum of 8.9% after the device was stored in a glove box for over 1400 h. The fascinating behavior is due to the slow crystal relaxation and surface passivation induced by EDAI₂. Another method of reducing lattice strain caused by a large organic cation is the addition of a smaller counter ion, such as Cs⁺. A small cation can fill point defects, reducing shallow trap states and protecting the sites from oxidation.[18] Using Cs⁺ to counterbalance the large GA⁺ cation in a FASnI₃ perovskite should allow the retention of the stabilizing effects of GA⁺ while reducing the local lattice strain, thus improving the performance of the corresponding devices.

In this study, we implement both GA⁺ and Cs⁺ cations into the FASnI₃ crystal structure to introduce more hydrogen bonding and to reduce local strains, respectively, within the perovskite crystals (Fig. 1a–d). We further incorporate EDAI₂ to replace some octahedral sites inside the crystal and to passivate defects at the grain boundaries (Fig. 1d) to relax lattice strains and reduce oxidation and trap states. We successfully synthesize densely packed, lead-free polycrystalline $(CsGA)_xFA_{1-2x}SnI_3$ films with EDAI₂. To reduce transport layer impacts on Sn oxidation, we use the inverted device structure of indium tin oxide (ITO)/poly(3,4-ethylenedioxythiophene):polystyrene sulfonate (PEDOT:PSS)/perovskite/[6,6]-phenyl-C₆₀-butyric acid methyl ester (PC₆₀BM)/2,9-dimethyl-7,7-diphenyl-1,10-phenanthroline (BCP)/Ag. The substitution of FA⁺ with the pair of Cs⁺ and GA⁺ leads to a $(CsGA)_{0.15}FA_{0.70}SnI_3$ device with a maximum PCE of 5.01%, much higher than that obtained simply by the incorporation of GA⁺ in $GA_{0.20}FA_{0.80}SnI_3$, but the device loses the diode behaviour after storage in a nitrogen-filled glove box for 30 days. With the EDAI₂ additive, freshly made $(CsGA)_{0.15}FA_{0.70}SnI_3$ with 1% EDAI₂ devices exhibit a record maximum PCE of 5.72%. The UV-Vis absorption and ultraviolet photoelectron spectroscopy (UPS) results show that the addition of EDAI₂ reduces the amount of trap states in perovskite thin films, improving the short-circuit current, J_{sc}, and the open-circuit voltage, V_{oc}. Devices made with $(CsGA)_{0.15}FA_{0.70}SnI_3$ and 1.5% EDAI₂ exhibit a maximum PCE of 5.69% and the maximum PCE increases to 6.39% after storage in a nitrogen-filled glove box for 4 days; the device retains 70% of the initial PCE after 45 days. Thin film trap state reduction and device stability improvement highlight the importance of EDAI₂ as a mitigating agent. Tuning cation sizes and integrating divalent cations create new routes for developing efficient and stable pure Sn PVSCs.

Experimental

Materials

Tin(II) iodide (SnI₂, 99.99%), cesium iodide (CsI, 99.999%), chloroform (≥99.99%), chlorobenzene (anhydrous, 99.8%), N,N-dimethyl sulfoxide (DMSO, anhydrous, ≥99.9%), 2-propanol and bathocuproine (BCP, 99.99%) were purchased
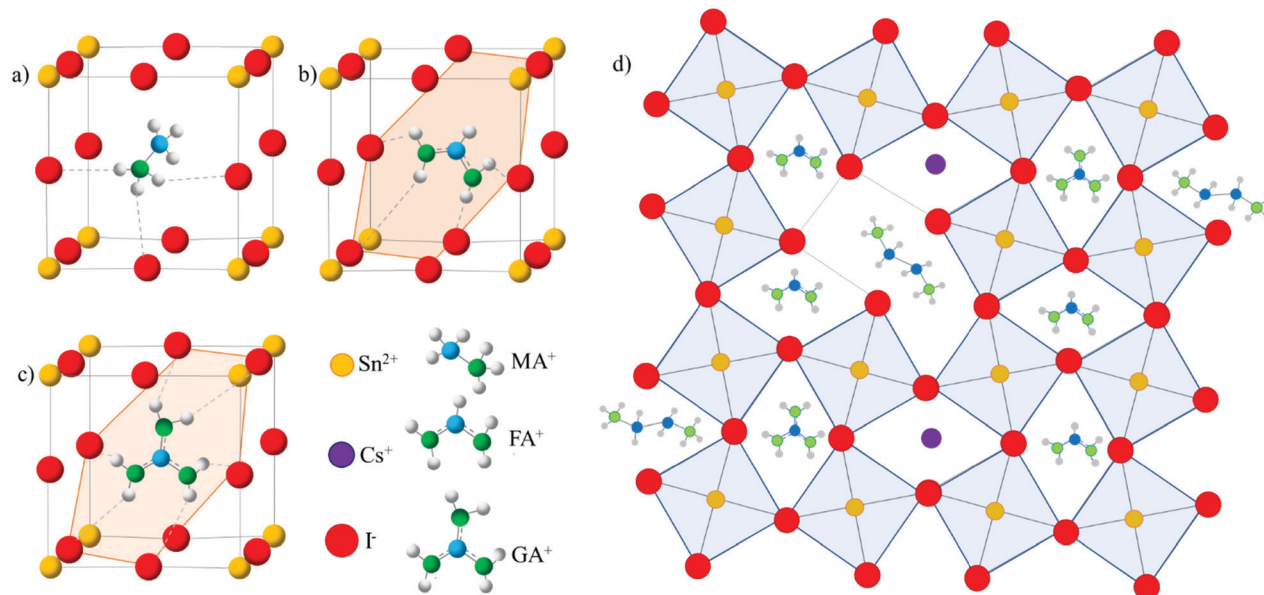
Fig. 1 SnI_6 inorganic framework highlighting N−H−I hydrogen bonding in (a) $MASnI_3$, (b) $FASnI_3$, and (c) $GASnI_3$. (d) Schematic illustration of the 3D $(CsGA)_xFA_{1-2x}SnI_3$ perovskite with the $EDAI_2$ additive showing EDA^{2+} cations creating potential hollowing inside the crystal as well as passivating defects along the grain boundaries. Yellow, purple, red, grey, blue, and green spheres represent Sn, Cs, I, H, C, and N atoms, respectively, and octahedra are marked by blue squares.

from Sigma-Aldrich (St. Louis, Missouri) without further purification. Guanidinium iodide (GAI) and formamidinium iodide (FAI) were purchased from GreatCell Solar (Queanbeyan, Australia) while ethylenediammonium diiodide ($EDAI_2$) was purchased from Millipore and used without further purification. [6,6]-Phenyl-C_{61}-butyric acid methyl ester ($PC_{60}BM$) ($>99.5\%$) was purchased from American Dye Solar (Quebec, Canada).

Thin film fabrication

The perovskite precursor solutions were prepared in a N_2 glove box by dissolving FAI and SnI_2 at the corresponding molar ratios in pure DMSO with a total concentration of 2.0 M. 10 mol% excess SnI_2 was added into the precursor solution to reduce vacancies. CsI, GAI, and $EDAI_2$ were dissolved in separate vials of DMSO at a concentration of 1.5 M and added to the perovskite precursor to achieve the correct triple cation composition. For the $(CsGA)_{0.15}FA_{0.70}SnI_3$ composition with 1% $EDAI_2$, for example, 0.1204 g of FAI and 0.4098 g of SnI_2 were dissolved in 850 μl of DMSO and stirred at 60 °C for 0.5 h. 100 μl of the 1.5 M CsI solution and 100 μl of the 1.5 M GAI solution were added to the precursor and stirred continuously at 60 °C for 0.5 h. 14 μl of the 1.5 M $EDAI_2$ solution was finally added to the precursor solution and stirred overnight at room temperature. The final precursor solution was then filtered through a 0.2 μm PTFE filter before use. Plain glass was cut into 15 mm × 15 mm substrates, which were cleaned *via* ultrasonication for 15 min in detergent in Millipore deionized water, Millipore deionized water, acetone, and isopropanol in sequence. The substrates were treated with oxygen plasma at 100 W for 10 min. A 70 μl drop of the precursor solution was spin-coated on a cleaned glass substrate at 500 rpm for 5 s,

1000 rpm for 15 s, and 4000 rpm for 40 s in a nitrogen glove box. 500 μl of chlorobenzene anti-solvent was dripped *in situ* onto the substrate during the last 15 s of the third spin-coating step. The perovskite films were then thermally annealed at 110 °C for 10 min.

Film characterization

Scanning electron microscopy (SEM) images were acquired using an FEI Sirion SEM operated at 15 kV to analyze the surface morphology. Two-dimensional X-ray diffraction (XRD) patterns were collected with a Bruker GADDS D8 Focus Powder Discover diffractometer using Cu Kα radiation (λ = 1.5419 Å) and the data were processed using the EVA package provided by Bruker AXS to investigate the crystalline structures of perovskite thin films. Ultraviolet-visible (UV-Vis) absorption spectra were collected using a Varian Cary 5000 UV-Vis-NIR spectrophotometer. Photoluminescence (PL) spectra were obtained with a Horiba HR-800 with 532 nm laser excitation. Ultraviolet photoelectron spectroscopy (UPS) measurements were conducted using a Kratos AXIS Ultra DLD spectrometer to investigate the valence band structures of perovskite thin films. A He discharge lamp source (Kratos) at an excitation energy of 21.2 eV was used in combination with a delay line detector at an electron pass energy of 5 eV. The UPS spectra for Au were acquired with a step size of 0.1 eV and a dwell time of 100 ms. The high-resolution UPS spectra and Fermi edge spectra were acquired with a step size of 0.01 eV and a dwell time of 100 ms.

Device fabrication

ITO coated glass substrates (10 Ohm sq^{-1} ITO, Colorado Concept Coatings LLC) were cut and cleaned as described

above. The PEDOT:PSS (AI 4083, Heraeus Clevios[TM]) solution was filtered with a 0.45 μm nylon filter. A 70 μl drop of PEDOT:PSS was spin-coated on a cleaned ITO coated glass substrate at 5000 rpm for 60 s and annealed at 150 °C for 10 min in air. The substrates were transferred to a N_2 glove box and the perovskite thin films were fabricated as described above. A $PC_{60}BM$ solution (15 mg ml^{-1} in chloroform) was then spin-coated on the perovskite films at 4000 rpm for 60 s and dried without annealing. A BCP solution (0.5 mg ml^{-1} in 2-propanol) was then spin-coated on the films at 4000 rpm for 60 s and dried without annealing. Finally, a mask with 3.14 × 10^{-6} m^2 area holes was placed on substrates that were loaded into a thermal evaporation chamber to thermally deposit 100 nm of silver as electrodes in a high vacuum evaporator (<1 × 10^{-6} Torr). The resulting device structure is ITO/PEDOT: PSS/perovskite/$PC_{60}BM$/BCP/Ag.

Device performance tests

The photocurrent density–voltage (J–V) curves, light intensity dependent J–V curves, and steady-state photocurrent measurements were conducted in a N_2 glove box with a Keithley 2400 SourceMeter and a Solar Light Co. Xenon lamp (16S–300 W) and AM 1.5G filter. Before measurements, the light intensity was calibrated to 100 mW cm^{-2} using a standardized National Renewable Energy Laboratory calibrated silicon solar cell.

Results and discussion

A one-step solution process with the chlorobenzene anti-solvent was used to form the pure Sn perovskite films. All precursors (FAI, SnI_2, GAI, CsI, and $EDAI_2$) were dissolved in pure DMSO to a total concentration of 2.0 M and spin-coated on ITO/glass substrates. 10 mol% excess SnI_2 was added to suppress the vacancies in the crystal lattice. All films were annealed at 110 °C for 10 min. The pure Sn perovskite films have the compositions of $(CsGA)_xFA_{1-2x}SnI_3 + y\%$ $EDAI_2$, where $x = 0.05, 0.10, 0.15$, and 0.20 and $y = 0, 0.5, 1.0, 1.5$, and 2.0. To simplify further discussion, we implement a notation of $(CsGA)_x$, where x is the percentage of cation added, to represent the various compositions. For example, $(CsGA)_5$ would represent $(CsGA)_{0.05}FA_{0.90}SnI_3$. The anti-solvent wash with the highly non-polar chlorobenzene was performed while spin-coating to remove excess DMSO from $SnI_2 \cdot 3DMSO$. The removal of excess DMSO results in the formation of A-SnI_2–2DMSO intermediates, allowing the slower removal of DMSO and growth of polycrystalline perovskite thin films upon annealing, thus minimizing pinholes. Although SnF_2 has been used to minimize the oxidation of Sn^{2+} to Sn^{4+}, excess SnF_2 has been shown to form separate phases and phase segregation on perovskite film surfaces or grain boundaries over time.[14,24] Excess SnI_2 has been shown to be effective in preventing Sn^{2+} oxidation by both compensating and suppressing Sn^{2+} vacancies without having any adverse side effects on phase stability and phase segregation.[25,26] Previous research has argued that excess SnI_2 may even be more effective than SnF_2 as a reducing agent since SnF_2 is hard to dissociate in films because of its low solubility and stability.[27] To minimize SnF_2 assisted phase segregation, we use excess SnI_2 plus $EDAI_2$ to reduce Sn^{2+} oxidation.

Fig. 2a shows the scanning electron microscopy (SEM) images of the synthesized $(CsGA)_{15} + y\%$ $EDAI_2$ perovskite thin films. Without the addition of $EDAI_2$, $(CsGA)_{15}$ films contain flat, large grains and pinholes, which may be due to the presence of a few nuclei and a rapid crystal growth rate.[28] $EDAI_2$ has been previously shown to act as a controlling agent and balance the kinetic processes between crystal growth and nucleation. The divalent nature of $EDAI_2$ allows uniform nucleation and, in tandem with the slow crystal growth, forming
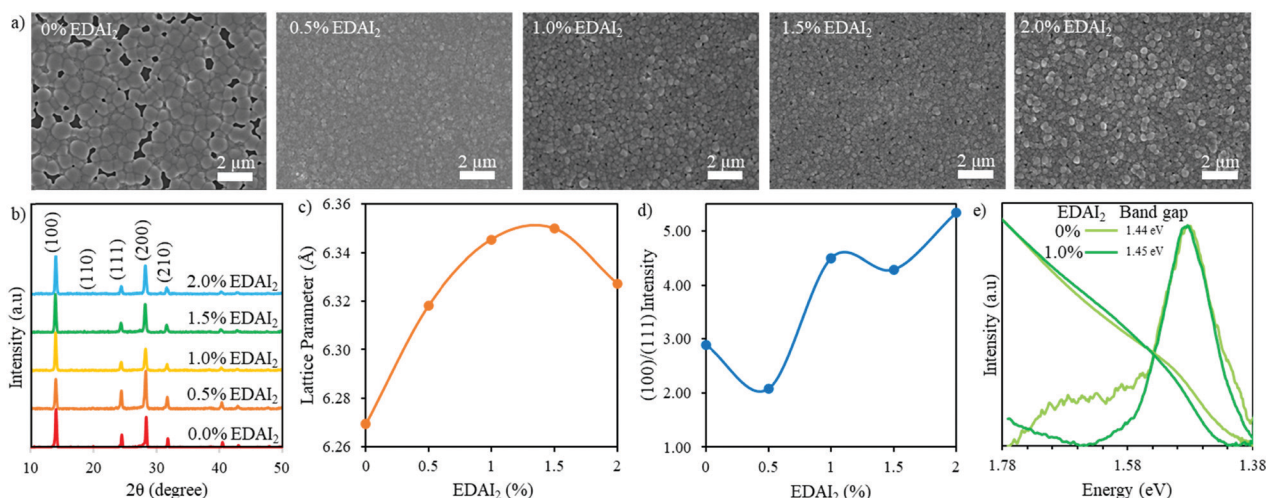

Fig. 2 (a) SEM images and (b) XRD patterns of $(CsGA)_{15} + y\%$ $EDAI_2$ perovskite thin films with $y = 0, 0.5, 1.0, 1.5$, and 2.0. (c) The cubic lattice parameter and (d) the (100)/(111) peak intensity ratio of $(CsGA)_{15} + y\%$ $EDAI_2$ as a function of percent $EDAI_2$. (e) PL spectra and normalized UV–Vis absorption spectra of $(CsGA)_{15}$ thin films with 0 and 1.0% $EDAI_2$. The optical band gaps are derived from the Tauc plots of $(CsGA)_{15}$ thin films with 0 and 1.0% $EDAI_2$ in Fig. S6e (ESI†).

densely packed perovskite films.[23] Because of this increased nucleation, from 0 to 1.0% EDAI$_2$, there is a decrease in grain size and the number of pinholes. Dense, small grains are formed for the (CsGA)$_{15}$ + 1.0% EDAI$_2$ film. Fig. S1a (ESI†) shows the corresponding SEM images for (CsGA)$_5$ + y% EDAI$_2$ and (CsGA)$_{10}$ + y% EDAI$_2$ perovskite thin films, which illustrate a similar trend of decreasing grain size and pinholes from 0 to 1.0% EDAI$_2$. When increasing EDAI$_2$ to 1.5% and 2%, the perovskite grains jut out from the surfaces, as shown in Fig. 2a for (CsGA)$_{15}$ and in Fig. S1a (ESI†) for the (CsGA)$_5$ and (CsGA)$_{10}$ films. This effect has been observed more drastically with 5% EDAI$_2$ incorporation, coupled with a decreased crystal density due to the replacement of B- and X-sites.[29] Fig. S2 (ESI†) shows the low magnification SEM images of all (CsGA)$_x$ + y% EDAI$_2$ films to demonstrate the consistency of film morphologies.

X-ray diffraction (XRD) was used to characterize the phase and crystallinity of the thin films. Fig. 2b shows the XRD patterns of (CsGA)$_{15}$ + 0–2.0% EDAI$_2$ thin films and the XRD patterns of (CsGA)$_5$ and (CsGA)$_{10}$ with the same range of EDAI$_2$ are shown in Fig. S1b (ESI†). A previous study reported a pseudo cubic orthorhombic phase for FASnI$_3$ with the *Amm*2 space group.[19] We compare the XRD pattern of the (CsGA)$_{15}$ + 1.0% EDAI$_2$ film and the simulated XRD patterns of FASnI$_3$ with the cubic *Pm*3*m* and orthorhombic *Amm*2 space groups in Fig. S3 (ESI†). The XRD pattern of the (CsGA)$_{15}$ + 1.0% EDAI$_2$ film matches very well with the peaks corresponding to the cubic phase and does not show any peak splitting or characteristic peaks of the orthorhombic phase. Kubicki *et al.* used NMR to obtain direct evidence of GA$^+$ incorporation into the MAPbI$_3$ and FAPbI$_3$ lattice forming phase-pure materials, dispelling the hypothesis that GA$^+$ is too large to enter the perovskite crystal structure.[30] We estimated the average A-site cation radii with mixed triple cations and calculated the Goldschmidt tolerance factors of (CsGA)$_x$FA$_{1-2x}$SnI$_3$ without EDAI$_2$ based on the average A-site cation radii (Table S1, ESI†). As the concentration of FA$^+$ (r = 2.53 Å) decreases and the concentrations of both Cs$^+$ (r = 1.67 Å) and GA$^+$ (r = 2.78 Å) increase, the average A-site cation radius decreases from 2.50 Å (CsGA)$_5$ to 2.47 Å (CsGA)$_{10}$ to 2.44 Å (CsGA)$_{15}$ (Table S1, ESI†). This trend is reflected in a decrease in the lattice parameter from 6.291 Å to 6.274 Å to 6.269 Å for (CsGA)$_5$, (CsGA)$_{10}$, and (CsGA)$_{15}$, respectively, with 0% EDAI$_2$ (Fig. 2c and Fig. S1c, ESI†), indicating the incorporation of CsGA into the perovskite crystal structures. The incorporation of CsGA suppresses the tolerance factor of FASnI$_3$, pushing the tolerance factor into the more ideal cubic region (Table S1, ESI†). Without EDAI$_2$, (CsGA)$_5$ and (CsGA)$_{10}$ have the tolerance factors of 0.992 and 0.986, respectively, approaching the tetragonal/hexagonal region. Small peaks emerging at 13.28° and 12.12° in the XRD patterns of (CsGA)$_5$ and (CsGA)$_{10}$ with 0% EDAI$_2$ thin films, respectively shown in Fig. S1b (ESI†), might be attributed to the orthorhombic impurity phase due to higher tolerance factors. No impurity phase peaks are present in the XRD pattern of the (CsGA)$_{15}$ thin film with 0% EDAI$_2$ because the tolerance factor has been pushed far enough into the ideal cubic region (Table S1, ESI†). Although further increasing the CsGA content can reduce the average A-site radii

and tolerance factors, both XRD patterns and SEM images show the formation of 2D guanidinium based perovskites and diminished 3D perovskites in (CsGA)$_{20}$ + 0–1.0% EDAI$_2$ thin films (Fig. S4, ESI†). With 0% EDAI$_2$, there are large sheets in the SEM images (Fig. S4b, ESI†) and diminished XRD peaks (Fig. S4a, ESI†), signifying a decrease in crystallinity. This crystallinity is improved when EDAI$_2$ is introduced but there is still a very large contaminant peak at 12.1°, which has previously been identified as a region with GA heavy 2D structures.[31]

The GA$_{0.20}$FA$_{0.80}$SnI$_3$ thin films showed a preferred growth direction along the (120) plane without EDAI$_2$ incorporation, which was altered to the (100) plane when 1% EDAI$_2$ was added.[15] We plotted the (100)/(111) peak intensity ratio as a function of percent added EDAI$_2$ for (CsGA)$_5$, (CsGA)$_{10}$ and (CsGA)$_{15}$ (Fig. 2d and Fig. S1d, ESI†). Our results show that, even without EDAI$_2$, the (CsGA)$_5$, (CsGA)$_{10}$ and (CsGA)$_{15}$ films exhibit a preferred (100) orientation with the (100)/(111) peak ratio increasing from 1.41 for (CsGA)$_5$ to 2.89 for (CsGA)$_{15}$, indicating that the incorporation of Cs$^+$ can alter the preferred orientation of crystal growth. The increasing (100) orientation may be due to the increased hydrogen bonding from GA$^+$ and the defect mitigation of Cs$^+$ allowing orientation to a more stable facet. The (100)/(111) peak intensity ratios increase with increasing addition of EDAI$_2$. This trend is particularly prominent for the (CsGA)$_{15}$ thin films because of a large decrease in the (111) peak intensity for the (CsGA)$_{15}$ thin films with 1.0–2.0% EDAI$_2$ (Fig. 2b and d). The (100) facet, which has an A–X or B–X layer termination, has been found to be most stable with the highest level of BX$_6$ coordination.[32] The EDAI$_2$ assisted growth of the (100) perovskite facet is due to hydrogen bonding and interactions with the halide cage. EDAI$_2$ then becomes the terminating end group and passivates the defects at the grain boundary, which is illustrated in Fig. 1d.

The effective ionic radius of EDAI$_2$ is estimated to be 3.74 Å.[29] Theoretically, the incorporation of EDAI$_2$ into the 3D structure of ABX$_3$ as an A-site replacement would increase the tolerance factor above 1, outside the optimum cubic range.[29] Previous XRD results showed that an orthorhombic phase FASnI$_3$ perovskite was transformed to a tetragonal phase with 39% EDAI$_2$ incorporation.[21] Because of the larger and divalent nature of EDAI$_2$, the cation not only takes the A-site but also hollows and protrudes into the space of the vacant B-site and displaces the X-site. This hollowing effect decreased the crystal density while maintaining the 3D crystal structure, which was confirmed by H-NMR.[29] We calculated the cubic phase lattice parameters of (CsGA)$_5$, (CsGA)$_{10}$ and (CsGA)$_{15}$ with different amounts of EDAI$_2$ added and plotted them as a function of percent EDAI$_2$ (Fig. 2c and Fig. S1c, ESI†). Fig. S1e (ESI†) shows the shift of the (100) peak for (CsGA)$_{15}$ with EDAI$_2$ addition from 0 to 2.0%. The changes in lattice parameter of (CsGA)$_5$, (CsGA)$_{10}$ and (CsGA)$_{15}$ thin films upon adding EDAI$_2$ relative to no EDAI$_2$ are plotted in Fig. S5 (ESI†). For the (CsGA)$_{15}$ films, the lattice parameter increases by 1.21% and 1.28% from 6.269 Å without EDAI$_2$ to 6.345 Å with 1% EDAI$_2$ and 6.350 Å with 1.5% EDAI$_2$. On further increasing EDAI$_2$ content to 2%, the lattice

parameter decreases to 6.327 Å when compared to the peak value with 1.5% $EDAI_2$ but still shows a 0.93% increase compared to that with 0% $EDAI_2$ (Fig. 2c and Fig. S5, ESI†). Similar trends were shown for $(CsGA)_5$ and $(CsGA)_{10}$ films, except that the lattice parameter decreases with 1.5% $EDAI_2$ and then increases with 2.0% $EDAI_2$ for both $(CsGA)_5$ and $(CsGA)_{10}$ films (Fig. S1c, ESI†). It is noted that negative lattice parameter changes were observed for $(CsGA)_5$ with 1.5 and 2.0% $EDAI_2$ and $(CsGA)_{10}$ with 1.5% $EDAI_2$ (Fig. S5, ESI†). Another interesting trend is that the lattice parameter increases with increasing CsGA substitution in thin films with 0.5 and 1.0% $EDAI_2$ addition. For $(CsGA)_5$ films, the lattice parameter increases similarly by 0.14% from 6.291 Å without $EDAI_2$ to 6.300 Å with 0.5% and 1% $EDAI_2$, while the corresponding increases are 0.57% and 0.71% from 6.274 Å without $EDAI_2$ to 6.31 Å with 0.5% $EDAI_2$ and 6.318 Å with 1% $EDAI_2$ for $(CsGA)_{10}$ films (Fig. S5, ESI†). The results indicate that EDA^{2+} ions are integrated into the crystal lattices, replacing octahedral sites in the perovskites and introducing a small "hollowing" effect, as illustrated in Fig. 1d. A stronger "hollowing" effect in the larger CsGA substitution films with the same small amount of $EDAI_2$ addition (0.5 and 1.0%) could be because the incorporation of a larger amount of small Cs^+ cations makes more A-site spaces to accommodate more EDA^{2+}, creating more hollow centers and expanding the crystal lattice. The decrease of the lattice parameter for both $(CsGA)_5$ and $(CsGA)_{10}$ films with 1.5% $EDAI_2$ could be due to expelling large GA^+ cations from the perovskite lattice and most EDA^{2+} being able to passivate or terminate, instead of hollow, the perovskite crystals. Although the lattice parameter for the $(CsGA)_{15}$ film with 2.0% $EDAI_2$ decreases compared to that of the film with 1.5% $EDAI_2$, the lattice parameter is still larger than that of the film without $EDAI_2$. This suggests that there might be an energy balance between hollowing crystal structures and terminating crystal surfaces with $EDAI_2$. Nonetheless, the results of increased crystal orientation towards the (100) plane and the lattice parameter variations with the addition of $EDAI_2$ reveal that $EDAI_2$ can both create hollow centers inside crystals and passivate grain boundaries.

To investigate the impacts of both CsGA and $EDAI_2$ on the optical and electronic properties, we recorded the UV-Vis absorption and static photoluminescence (PL) spectra of $(CsGA)_5$, $(CsGA)_{10}$ and $(CsGA)_{15}$ thin films. The UV-Vis and PL spectra of $(CsGA)_5$, $(CsGA)_{10}$ and $(CsGA)_{15}$ thin films with 0 and 1% $EDAI_2$ addition are shown in Fig. 2e and Fig. S6 (ESI†). The optical band gaps derived from the Tauc plots in Fig. S6c–e (ESI†) for 0 and 1% $EDAI_2$ contents are 1.46 and 1.46 eV for $(CsGA)_5$, 1.45 and 1.46 eV for $(CsGA)_{10}$, and 1.44 and 1.45 eV for $(CsGA)_{15}$, respectively. Without $EDAI_2$, the band gap decreases slightly from 1.46 to 1.45 eV when increasing the CsGA substitution from 5 to 15%. The average cation radius and lattice parameter decrease for these films, as discussed above (Fig. 2c and Table S1, Fig. S1c, ESI†). In our previous work, we showed that the band gap of $Cs_x(MA_{0.17}FA_{0.83})_{1-x}Sn(I_{0.83}Br_{0.17})_3$ perovskites decreases with decreasing lattice parameter due to a smaller average cation radius.[33] Both A-site induced BX_6 octahedral tilting and B–X overlap on the conduction and valence band edges of perovskites influence these band gap trends.[34]

The correlation between the band gap decrease and the lattice parameter decrease for $(CsGA)_x$ without $EDAI_2$ reflects that the same mechanism is occurring, where the increased isotropic lattice constrictions and B–X overlap make the valence band maximum shift upwards more than the conduction band minimum.[35] For $(CsGA)_{10}$ and $(CsGA)_{15}$, when 1% $EDAI_2$ is added, there is a 0.01 eV blue shift of band gaps because of the decreased isotropic lattice constrictions, decreasing the B–X overlap. This blue shift is also due to the larger and divalent nature of EDA^{2+} displacing B-site and X-site atoms, eliminating several B–X connections. These missing B–X connections decrease the orbital overlap of the remaining Sn–I bonds, narrowing the width of the valence band and conduction band.[22,23] In addition, the UV-Vis absorption cutoff edges are sharper and the PL peaks are narrower and stronger for $(CsGA)_{10}$ and $(CsGA)_{15}$ with 1.0% $EDAI_2$. These phenomena are more obvious with increasing CsGA substitution and diminish for $(CsGA)_5$ films (Fig. 2e and Fig. S6, ESI†). Although there is still a difference in band gap with and without $EDAI_2$ for the $(CsGA)_5$ composition, the change is small enough that they are considered the same band gap within our measurement limitations. The opening of the band gap, sharpening of the UV-Vis absorption cutoff edge, and narrowing with increased intensity of the PL peak further suggest that the addition of $EDAI_2$ can reduce the trap states between band gaps by reducing point defects inside the crystals via the hollowing effect and by reducing surface defects via the passivation of grain boundaries. Moreover, a greater amount of CsGA substitution is crucial for integrating EDA^{2+} cations and utilizing their effect on decreasing trap states.

The $(CsGA)_x + y\%$ $EDAI_2$ films were deployed as active layers in PVSCs with an inverted device structure of ITO/PEDOT:PSS/perovskite/$PC_{60}BM$/BCP/Ag, which is illustrated in the cross-sectional SEM image shown in Fig. 3a. Solution processed PEDOT:PSS acts as the hole transport layer (HTL) while the spin-coated $PC_{60}BM$ acts as the electron transport layer (ETL) as well as reducing the surface roughness and passivating possible traps.[36] The solution processed BCP layer acts as a hole blocking layer (HBL) to increase charge separation and minimize recombination. Fig. 3b shows the photocurrent density–voltage (J–V) characteristics of the devices fabricated with $(CsGA)_{15} + y\%$ $EDAI_2$ active layers with y = 0, 0.5, 1.0, 1.5 and 2.0. Detailed photovoltaic parameters are summarized in Table 1. The J–V characteristics and detailed photovoltaic parameters of the devices fabricated with $(CsGA)_5$ and $(CsGA)_{10}$ with 0–2.0% $EDAI_2$ are presented in Fig. S7 and Table S2 (ESI†). The devices containing the active layer $(CsGA)_{15}$ without $EDAI_2$ exhibit the maximum PCE of 5.01%, with the corresponding V_{oc} of 0.32 V, J_{sc} of 22.61 mA cm^{-2}, and FF of 0.70. The maximum PCE of our $(CsGA)_{15} + 0\%$ $EDAI_2$ devices is much higher than the 0.5% PCE of the devices with $GA_{0.2}FA_{0.8}SnI_3$ without $EDAI_2$, particularly, the maximum V_{oc} of 0.32 V versus the reported V_{oc} of ~0.1 V.[15] Adding Cs^+ to balance the larger GA^+ cations could decrease shallow trap states via Cs^+ filling in defects, which increases V_{oc} and improves J_{sc} and FF, culminating in much better device performance. Adding 0.5 and 1.0% $EDAI_2$ increases the maximum PCE to 5.39% and 5.72% due to both
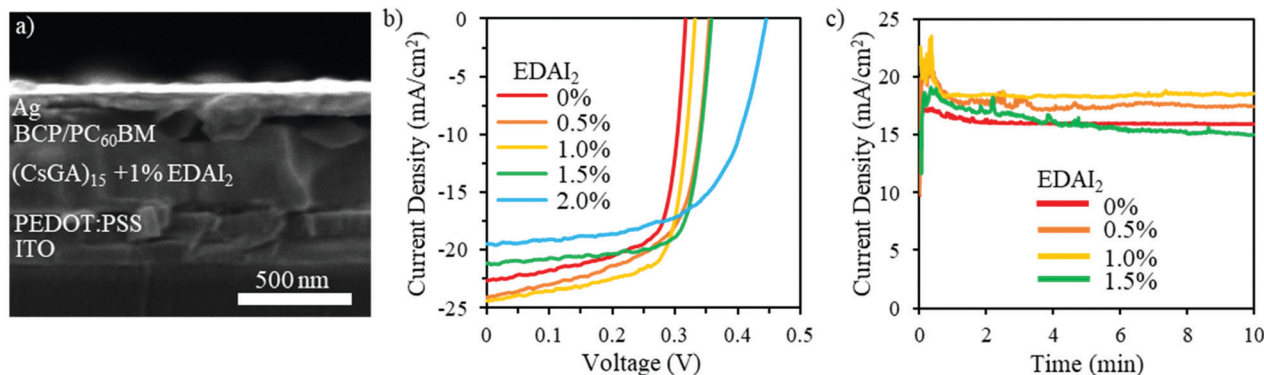
Fig. 3 (a) Cross-sectional SEM image showing the $(CsGA)_{15}$ + 1.0% $EDAI_2$ PVSC with the following layers: ITO (200 nm)/PEDOT:PSS (50 nm)/perovskite (400 nm)/$PC_{60}BM$/BCP/Ag (100 nm). (b) Photocurrent density–voltage (J–V) characteristics of the best performance PVSCs with the active layer containing $(CsGA)_{15}$ + y% $EDAI_2$ thin films with y = 0, 0.5, 1.0, 1.5, and 2.0 under AM 1.5G illumination scanned from −0.1 to 0.6 V at a scan rate of 0.01 V s^{-1}. (c) Steady state photocurrent for the best performance PVSCs containing the active layers of $(CsGA)_{15}$ at the maximum power points with the voltages of 0.274, 0.290, 0.272, and 0.308 V for 0, 0.5, 1.0, and 1.5% $EDAI_2$, respectively.

Table 1 Average photovoltaic parameters and the best performance device photovoltaic parameters in parentheses along with series resistance, R_s, and shunt resistance, R_{sh}, of PVSCs containing $(CsGA)_{15}$ + y% $EDAI_2$ with y = 0, 0.5, 1.0, 1.5, and 2.0 measured under AM 1.5G illumination obtained from the forward J–V measurements

Device	V_{oc} (V)	J_{sc} (mA cm^2)	FF	PCE (%)	R_s (Ω cm^2)	R_{sllh} (Ω cm^2)
$(CsGA)_{15}$ + 0%	0.30 ± 0.02 (0.32)	20.84 ± 3.31 (22.61)	0.71 ± 0.01 (0.70)	4.45 ± 0.87 (5.01)	2.40	64.46
$(CsGA)_{15}$ + 0.5%	0.35 ± 0.02 (0.35)	21.43 ± 2.28 (24.03)	0.61 ± 0.04 (0.63)	4.58 ± 0.61 (5.39)	4.22	66.59
$(CsGA)_{15}$ + 1.0%	0.35 ± 0.02 (0.33)	20.81 ± 1.78 (24.32)	0.63 ± 0.06 (0.71)	4.62 ± 0.63 (5.72)	2.72	78.00
$(CsGA)_{15}$ + 1.5%	0.38 ± 0.01 (0.36)	20.23 ± 1.18 (21.16)	0.66 ± 0.06 (0.75)	5.05 ± 0.53 (5.69)	3.05	133.92
$(CsGA)_{15}$ + 2.0%	0.43 ± 0.02 (0.45)	15.20 ± 2.50 (19.53)	0.57 ± 0.04 (0.62)	3.74 ± 0.94 (5.40)	6.67	92.14

the increased V_{oc} of 0.35 and 0.33 V, and J_{sc} of 24.03 and 24.32 mA cm^{-2}, respectively. Adding 1.5% $EDAI_2$ further increases V_{oc} to 0.36 V and particularly increases the FF to 0.75, maintaining a high maximum PCE of 5.69%. The high FF may be due to the increasing Shunt resistance, R_{sh}, from 64.46 Ω cm^2 with 0% $EDAI_2$ to 133.92 Ω cm^2 with 1.5% $EDAI_2$. When adding 2.0% $EDAI_2$, although V_{oc} increases to the largest value of 0.45 V, the lowest J_{sc} of 19.53 mA cm^{-2} and the FF of 0.62 decrease the maximum PCE slightly to 5.40%. The lowest J_{sc} may be due to an increase in series resistance, R_s, to the maximum of 6.67 Ω cm^2 among all $(CsGA)_{15}$ devices. Fig. 3c shows that the photocurrent at the maximum power point *versus* time for the $(CsGA)_{15}$ + 0–1.5% $EDAI_2$ devices remained stable under illumination in an inert atmosphere for the 10 min test period. The better performance exhibited by $(CsGA)_{15}$ devices with 0.5–1.5% $EDAI_2$ could be due to the benefits of improved film quality, (100) plane dominated termination, and reduced trap states. The declined performance of $(CsGA)_{15}$ with 2.0% $EDAI_2$ could be due to the rough surface, creating more interface trap states. PVSCs based on active layers of $(CsGA)_5$ and $(CsGA)_{10}$ with 0–2% $EDAI_2$ exhibit lower maximum PCEs compared to their counterparts of $(CsGA)_{15}$ mainly because of the lower J_{sc} and FF values. This could be attributed to the presence of more pinholes and impurity phases in the perovskite films, resulting in a higher R_s and lower R_{sh}.

A previous study has shown that devices based on $GA_{0.20}FA_{0.80}SnI_3$ with 1% $EDAI_2$ active layers exhibited a V_{oc} of 0.619 V compared to 0.49 V for the devices based on $FASnI_3$

with 1% $EDAI_2$ active layers because of the downshifted valence band maximum to −5.20 eV *versus* −4.92 eV, which aligns better with the work function of PEDOT:PSS (−5.2 eV) as the HTL. The V_{oc} values of our devices are low compared to the reported V_{oc} values. To further investigate this, we conducted ultraviolet photoelectron spectroscopy (UPS) analysis of $(CsGA)_5$, $(CsGA)_{10}$ and $(CsGA)_{15}$ films with 1.5% $EDAI_2$ because the devices based on these films exhibit high performance. Fig. 4a shows the energy diagram of the materials involved in the devices. The valence band maxima (VBMs) of $(CsGA)_5$, $(CsGA)_{10}$ and $(CsGA)_{15}$ with 1.5% $EDAI_2$ were obtained from their UPS spectra (Fig. S8, ESI†) and the conduction band minima (CBMs) were estimated from the VBMs and the optical band gaps determined from the UV-Vis spectra of the $(CsGA)_5$, $(CsGA)_{10}$ and $(CsGA)_{15}$ films with 1.0% $EDAI_2$. The VBMs are determined to be −5.08, −5.07 and −5.16 eV for $(CsGA)_5$, $(CsGA)_{10}$ and $(CsGA)_{15}$ with 1.5% $EDAI_2$, respectively. All of them are unfavorable for hole transport with the PEDOT:PSS HTL,[15] which could lead to low V_{oc} values. The deepest VBM and the smallest band gap of $(CsGA)_{15}$ make the CBM downshift to −3.73 eV. Both the downshifted VBM and CBM of $(CsGA)_{15}$ enable the best energy alignment with the HTL and ETL, respectively, which could explain the best performance of devices based on $(CsGA)_{15}$ films. The $(CsGA)_5$, $(CsGA)_{10}$ and $(CsGA)_{15}$ films with 1.5% $EDAI_2$ have a Fermi level 0.4 eV above the VBM, indicating the p-type doping of all these perovskites (Fig. 4b). Previous studies have shown that guanidinium

Fig. 4 (a) Band energy diagram of PVSCs with $(CsGA)_x$ + 1.5% $EDAI_2$ active layers, where x = 5, 10 and 15. The band gaps derived from the UV-Vis spectra are indicated. (b) Energy level scheme for the $(CsGA)_5$, $(CsGA)_{10}$ and $(CsGA)_{15}$ films with 1.5% $EDAI_2$ based on the parameters derived from the UPS spectra.

addition in $MAPbI_3$ converts the perovskite to a p-type semi-conductor with the Fermi level shifting from 1.1 to 0.89 eV above the VBM for $MAPbI_3$ and $GA_{0.25}MA_{0.75}PbI_3$, respectively.[37] X-site anion interstitial (X_i), A-site and B-site vacancy (V_A and V_B), and antisite (A_B, X_A and X_B) point defects typically lead to p-type perovskites.[21] Sn-based perovskites tend to be p-type due to self-doping by Sn^{4+}.[38] The p-type nature of the $(CsGA)_{15}$ film with 1.5% $EDAI_2$ could be due to $EDAI_2$ having a "hollowing" impact on the perovskite structure, giving the increased lattice parameter (Fig. 2c). $EDAI_2$ has been shown to favor replacing octahedral cages with the B-site and the X-site and these metal and halide defects (vacancies and antisites) contribute to a more p-type perovskite.[19,29,39] Since the lattice parameters of $(CsGA)_5$ and $(CsGA)_{10}$ films with 1.5% $EDAI_2$ are even smaller than those without $EDAI_2$ because of the possibility of expelling GA^+ cations, A-site vacancies could be formed in these perovskites besides the aforementioned point defects, resulting in p-type perovskites.

Balanced charge generation, recombination and extraction rates are key factors in determining solar cell performance.[40] Charge recombination results in loss of photogenerated charges, lowering J_{sc} and FF. The maximum V_{oc} of a solar cell can be achieved when all photogenerated charges recombine solely radiatively.[41] To understand device performance related to the mitigation of defects by incorporating $EDAI_2$ in $(CsGA)_{15}$ perovskites, we investigated the evolution of V_{oc}, J_{sc} and FF as a function of light intensity for $(CsGA)_{15}$ with 0–1.5% $EDAI_2$. The V_{oc} of light intensity is an independent exploration of recombination compared to that of J_{sc} and FF. The current is zero under open-circuit conditions with all photogenerated carriers recombining within the cell. Recombination studies near the open-circuit are, therefore, particularly sensitive to recombination mechanisms and the impact of shallow traps. The open-circuit

voltage shows a logarithmic dependence on light intensity with a slope of nk_BT/q, where n represents different recombination mechanisms, k_B is the Boltzmann constant, T is the absolute temperature, and q is the elementary charge. When $n > 2$, monomolecular recombination dominates and trap states play a significant role, while when $n \sim 1$, bimolecular recombination dominates, demonstrating minimal shallow trap states in the perovskites.[42] The V_{oc} versus logarithmic scale light intensity plots for $(CsGA)_{15}$ devices show that the slope changes from greater than 2 to close to 1 from no $EDAI_2$ addition to 1.0 and 1.5% $EDAI_2$ addition (Fig. 5a), indicating charge carrier recombination from monomolecular, trap-state assisted recombination to biomolecular recombination. These results are consistent with the trap-state reduction shown by the UV-Vis and PL spectra, which further supports the hypothesis that $EDAI_2$ has a hollowing effect, reducing bulk defects.

Fig. 5b shows the double logarithmic scale with the relation of J_{sc} versus light intensity. For the power law dependence of J_{sc} on light intensity ($J_{sc} \propto I^\alpha$), the deviation from unity of the slope implies bimolecular recombination. When α is less than 1, this could be a result of bimolecular recombination, variations in both carrier mobilities, or distribution in the density of states. When $\alpha \sim 0.75$, space charge effects might be induced by the interfacial layers. When $\alpha = 1$, there are no space charge effects and all carriers are swept out prior to recombination.[42,43] For $EDAI_2$ addition from 0% to 1.5%, α values change from 1.21 to 1.00. This shows that the addition of $EDAI_2$ reduces the deep trap states by passivating grain boundaries and charge carriers are effectively extracted. We also plotted FF as a function of logarithmic scale light intensity (Fig. 5c). These FF trends show the different capabilities of the perovskite materials to support balanced charge carrier generation and extraction over this range of light intensities.
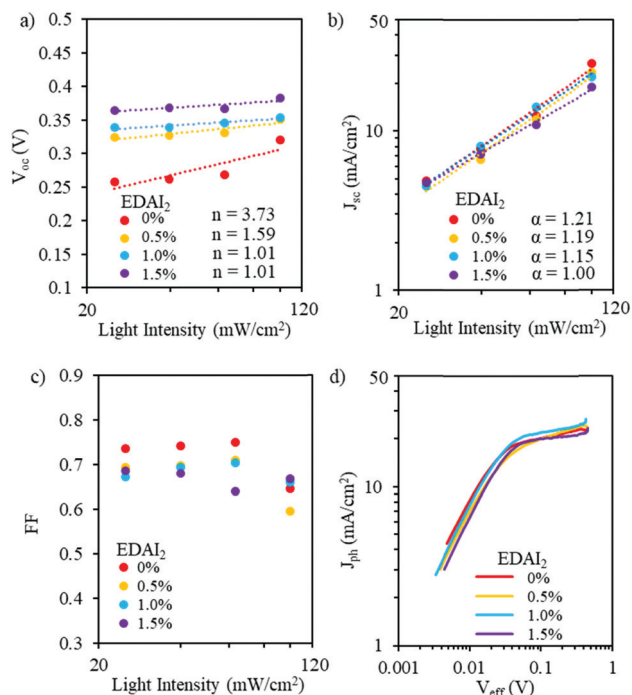
Fig. 5 (a) V_{oc}, (b) J_{sc}, and (c) FF as a function of light intensity and (d) photocurrent density as a function of effective voltage for PVSCs with $(CsGA)_{15}$ + 0–1.5% $EDAI_2$.

At low light intensities, the $(CsGA)_{15}$ device without $EDAI_2$ shows a higher FF compared to the devices with 0.5–1.5% $EDAI_2$, indicating that, despite the trap states, low density

charge carriers in $(CsGA)_{15}$ + 0% $EDAI_2$ are still able to be extracted due to the high intrinsic charge carrier mobility and long diffusion length of perovskites.[44,45] When the light intensity increases to 1 sun, 100 mW cm^{-2}, more charge carriers are recombined *via* trap states, leading to a significant decrease of FF for $(CsGA)_{15}$ with 0 and 0.5% $EDAI_2$. The $(CsGA)_{15}$ device with 1.5% $EDAI_2$ retains the same level of FF at 1 sun illumination, demonstrating the reduction of trap states by adding $EDAI_2$. To elucidate whether the FF reduction under 1 sun illumination for the $(CsGA)_{15}$ devices without $EDAI_2$ and those with 0.5–1% $EDAI_2$ is due to the charge extraction limit, we explored the photocurrent density (J_{ph}) as a function of effective voltage (V_{eff}). J_{ph} is defined as $J_{ph} = J_1 - J_d$, where J_1 and J_d represent the current densities under light and dark conditions, respectively. V_{eff} is defined as $V_{eff} = V_0 - V$, where V_0 is the compensation voltage defined as $J_{ph}(V_0) = 0$ and V is the applied voltage.[40] Fig. 5d shows that, for all devices, photocurrent densities under 1 sun illumination reach saturation at a similar low effective voltage ~ 0.05 V, suggesting that charge extraction is not a limiting factor. The low saturation effective voltage could be linked to the better band alignment of $(CsGA)_{15}$ with the charge selective layers (Fig. 4a).

To determine the impact of mixing CsGA with FA at the A-site and adding $EDAI_2$ on the stability of pure Sn perovskite solar cells, long-term device stability in an inert environment was evaluated. Fig. 6 shows the normalized V_{oc}, J_{sc}, FF, and PCE of $(CsGA)_{15}$ + 0–1.5% $EDAI_2$ devices over 45 days in an inert nitrogen atmosphere. The devices with 0% $EDAI_2$ show a decrease of all photovoltaic parameters over time and after 30 days show a short-circuited behavior. This short-circuited

Fig. 6 Normalized (a) V_{oc}, (b) J_{sc}, (c) FF, and (d) PCE of the devices containing the active layers of $(CsGA)_{15}$ + 0–1.5% $EDAI_2$ over time in a nitrogen-filled glove box. The $(CsGA)_{15}$ + 0% $EDAI_2$ devices showed a short-circuited behavior after 30 days.

behavior is due to highly oxidized Sn^{4+}, which has been shown to create metal-like conductivity in perovskite solar cells.[46] The addition of $EDAI_2$ greatly increased the device stability, further demonstrating the point defect reducing capability of $EDAI_2$ by hollowing crystal structures and passivating grain boundaries. In the case of 0.5–1.5% $EDAI_2$ addition, Fig. 6 shows that V_{oc} is very stable while J_{sc} and FF briefly increase during storage. The performance of the $(CsGA)_{0.15}FA_{0.70}SnI_3$ device with 1.5% $EDAI_2$ shows an increase in maximum PCE from 5.69 to 6.39% after 5 days of storage. Previously, with $GA_{0.2}FA_{0.8}SnI_3$ perovskite films and 1% $EDAI_2$, the efficiency also increased in storage as well.[15] Since this phenomenon only occurs with $EDAI_2$ addition in our research and mostly impacts J_{sc}, this shows that there is an increased amount of grain passivation over time. $EDAI_2$ is successfully able to prevent oxidation, maintaining these photovoltaic parameters.

Conclusion

In summary, the addition of Cs^+ and GA^+ into $FASnI_3$ was implemented to utilize the high hydrogen bonding capability of the GA^+ organic cation while relaxing the local lattice strain and filling point defects with a smaller Cs^+ counter cation. The $EDAI_2$ additive not only yielded pinhole-free cubic phase $(CsGA)_xFA_{1-2x}SnI_3$ perovskite films but also decreased both shallow and deep trap states in the perovskite films. With increased CsGA substitution, the relaxed strain allowed more integration of $EDAI_2$ into the crystal structure, increasing these positive impacts. The devices with $(CsGA)_{0.15}FA_{0.70}SnI_3$ and 0–2% $EDAI_2$ all achieved a maximum PCE higher than 5% with the highest of 5.72% for a fresh device with $(CsGA)_{0.15}FA_{0.70}SnI_3$ and 1% $EDAI_2$. After storage, the maximum PCE was increased from 5.69 to 6.39% for the $(CsGA)_{0.15}FA_{0.70}SnI_3$ and 1.5% $EDAI_2$ devices. The devices with the $EDAI_2$ additive showed better long-term stability compared to those without $EDAI_2$. Overall, this study demonstrates cation tuning to integrate stabilizing factors into pure Sn perovskites, creating potential routes for further improving lead-free devices in the future.

Conflicts of interest

The authors declare no conflict of interest.

Acknowledgements

References

1 NREL, Best Research-Cell Efficiency Chart, https://www.nrel.gov/pv/cell-efficiency.html.

2 Q. Chen, N. De Marco, Y. Yang, T. Bin Song, C. C. Chen, H. Zhao, Z. Hong, H. Zhou and Y. Yang, *Nano Today*, 2015, **10**, 355–396.

3 S. Chatterjee and A. J. Pal, *J. Mater. Chem. A*, 2018, **6**, 3793–3823.

4 G. Nasti and A. Abate, *Adv. Energy Mater.*, 2019, **13**, 1–16.

5 H. Yao, F. Zhou, Z. Li, Z. Ci, L. Ding and Z. Jin, *Adv. Sci.*, 2020, 1903540.

6 K. Liang, D. B. Mitzi and M. T. Prikas, *Chem. Mater.*, 1998, **10**, 403–411.

7 T. Leijtens, R. Prasanna, A. Gold-Parker, M. F. Toney and M. D. McGehee, *ACS Energy Lett.*, 2017, **2**, 2159–2165.

8 W. Ke and M. G. Kanatzidis, *Nat. Commun.*, 2019, **10**, 1–4.

9 C. C. Stoumpos, C. D. Malliakas and M. G. Kanatzidis, *Inorg. Chem.*, 2013, **52**, 9019–9038.

10 M. Konstantakou and T. Stergiopoulos, *J. Mater. Chem. A*, 2017, **5**, 11518–11549.

11 Z. Chen, C. Yu, K. Shum, J. J. Wang, W. Pfenninger, N. Vockic, J. Midgley and J. T. Kenney, *J. Lumin.*, 2012, **132**, 345–349.

12 N. K. Noel, S. D. Stranks, A. Abate, C. Wehrenfennig, S. Guarnera, A. A. Haghighirad, A. Sadhanala, G. E. Eperon, S. K. Pathak, M. B. Johnston, A. Petrozza, L. M. Herz and H. J. Snaith, *Energy Environ. Sci.*, 2014, **7**, 3061–3068.

13 F. Hao, C. C. Stoumpos, D. H. Cao, R. P. H. Chang and M. G. Kanatzidis, *Nat. Photonics*, 2014, **8**, 489–494.

14 W. Liao, D. Zhao, Y. Yu, C. R. Grice, C. Wang, A. J. Cimaroli, P. Schulz, W. Meng, K. Zhu, R. G. Xiong and Y. Yan, *Adv. Mater.*, 2016, **28**, 9333–9340.

15 E. Jokar, C. H. Chien, C. M. Tsai, A. Fathi and E. W. G. Diau, *Adv. Mater.*, 2019, **31**, 1–7.

16 S. Kanno, Y. Imamura and M. Hada, *J. Phys. Chem. C*, 2018, **122**, 15966–15972.

17 N. De Marco, H. Zhou, Q. Chen, P. Sun, Z. Liu, L. Meng, E. P. Yao, Y. Liu, A. Schiffer and Y. Yang, *Nano Lett.*, 2016, **16**, 1009–1016.

18 M. I. Saidaminov, J. Kim, A. Jain, R. Quintero-Bermudez, H. Tan, G. Long, F. Tan, A. Johnston, Y. Zhao, O. Voznyy and E. H. Sargent, *Nat. Energy*, 2018, **3**, 648–654.

19 W. Ke, C. C. Stoumpos, M. Zhu, L. Mao, I. Spanopoulos, J. Liu, O. Y. Kontsevoi, M. Chen, D. Sarma, Y. Zhang,

M. R. Wasielewski and M. G. Kanatzidis, *Sci. Adv.*, 2017, **3**, 1–10.

20 Z. Ni, C. Bao, Y. Liu, Q. Jiang, W. Q. Wu, S. Chen, X. Dai, B. Chen, B. Hartweg, Z. Yu, Z. Holman and J. Huang, *Science*, 2020, **367**, 1352–1358.

21 H. Jin, E. Debroye, M. Keshavarz, I. G. Scheblykin, M. B. J. Roeffaers, J. Hofkens and J. A. Steele, *Mater. Horiz.*, 2020, **7**, 397–410.

22 I. Spanopoulos, W. Ke, C. C. Stoumpos, E. C. Schueller, O. Y. Kontsevoi, R. Seshadri and M. G. Kanatzidis, *J. Am. Chem. Soc.*, 2018, **140**, 5728–5742.

23 E. Jokar, C. H. Chien, A. Fathi, M. Rameez, Y. H. Chang and E. W. G. Diau, *Energy Environ. Sci.*, 2018, **11**, 2353–2362.

24 S. J. Lee, S. S. Shin, Y. C. Kim, D. Kim, T. K. Ahn, J. H. Noh, J. Seo and S. Il Seok, *J. Am. Chem. Soc.*, 2016, **138**, 3974–3977.

25 T. Bin Song, T. Yokoyama, S. Aramaki and M. G. Kanatzidis, *ACS Energy Lett.*, 2017, **2**, 897–903.

26 T. Wang and F. Yan, *Chem. – Asian J.*, 2020, **15**, 1524–1535.

27 Z. Zhu, C. C. Chueh, N. Li, C. Mao and A. K. Y. Jen, *Adv. Mater.*, 2018, **30**, 1–9.

28 Q. Q. Ge, J. Ding, J. Liu, J. Y. Ma, Y. X. Chen, X. X. Gao, L. J. Wan and J. S. Hu, *J. Mater. Chem. A*, 2016, **4**, 13458–13467.

29 W. Ke, I. Spanopoulos, Q. Tu, I. Hadar, X. Li, G. S. Shekhawat, V. P. Dravid and M. G. Kanatzidis, *J. Am. Chem. Soc.*, 2019, **141**, 8627–8637.

30 D. J. Kubicki, D. Prochowicz, A. Hofstetter, M. Saski, P. Yadav, D. Bi, N. Pellet, J. Lewiński, S. M. Zakeeruddin, M. Grätzel and L. Emsley, *J. Am. Chem. Soc.*, 2018, **140**, 3345–3351.

31 W. Zhang, J. Xiong, J. Li and W. A. Daoud, *J. Mater. Chem. A*, 2019, **7**, 9486–9496.

32 K. Huang, L. Yuan and S. Feng, *Inorg. Chem. Front.*, 2015, **2**, 965–981.

33 G. A. Tosado, Y. Y. Lin, E. Zheng and Q. Yu, *J. Mater. Chem. A*, 2018, **6**, 17426–17436.

34 J. H. Lee, N. C. Bristowe, J. H. Lee, S. H. Lee, P. D. Bristowe, A. K. Cheetham and H. M. Jang, *Chem. Mater.*, 2016, **28**, 4259–4266.

35 R. Prasanna, A. Gold-Parker, T. Leijtens, B. Conings, A. Babayigit, H. G. Boyen, M. F. Toney and M. D. McGehee, *J. Am. Chem. Soc.*, 2017, **139**, 11117–11124.

36 Y. Shao, Z. Xiao, C. Bi, Y. Yuan and J. Huang, *Nat. Commun.*, 2014, **5**, 1–7.

37 D. Prochowicz, M. M. Tavakoli, A. Q. Alanazi, S. Trivedi, H. Tavakoli Dastjerdi, S. M. Zakeeruddin, M. Grätzel and P. Yadav, *ACS Omega*, 2019, **4**, 16840–16846.

38 E. W. G. Diau, E. Jokar and M. Rameez, *ACS Energy Lett.*, 2019, **4**, 1930–1937.

39 W. Ke, C. C. Stoumpos, I. Spanopoulos, L. Mao, M. Chen, M. R. Wasielewski and M. G. Kanatzidis, *J. Am. Chem. Soc.*, 2017, **139**, 14800–14806.

40 J. Troughton, N. Gasparini and D. Baran, *J. Mater. Chem. A*, 2018, **6**, 21913–21917.

41 W. Shockley and H. J. Queisser, *J. Appl. Phys.*, 1961, **32**, 510–519.

42 S. R. Cowan, A. Roy and A. J. Heeger, *Phys. Rev. B: Condens. Matter Mater. Phys.*, 2010, **82**, 1–10.

43 S. Shao, Z. Chen, H. H. Fang, G. H. Ten Brink, D. Bartesaghi, S. Adjokatse, L. J. A. Koster, B. J. Kooi, A. Facchetti and M. A. Loi, *J. Mater. Chem. A*, 2016, **4**, 2419–2426.

44 L. M. Herz, *ACS Energy Lett.*, 2017, **2**, 1539–1548.

45 S. D. Stranks, G. E. Eperon, G. Grancini, C. Menelaou, M. J. P. Alcocer, T. Leijtens, L. M. Herz, A. Petrozza and H. J. Snaith, *Science*, 2013, **342**, 341–345.

46 I. Chung, J. H. Song, J. Im, J. Androulakis, C. D. Malliakas, H. Li, A. J. Freeman, J. T. Kenney and M. G. Kanatzidis, *J. Am. Chem. Soc.*, 2012, **134**, 8579–8587.